ACS APPLIED MATERIALS & INTERFACES

www.acsami.org

Research Article

# Systematic Design of a Graphene Ink Formulation for Aerosol Jet Printing

Livio Gamba, Zachary T. Johnson, Jackie Atterberg, Santiago Diaz-Arauzo, Julia R. Downing, Jonathan C. Claussen, Mark C. Hersam, and Ethan B. Secor*

Cite This: *ACS Appl. Mater. Interfaces* 2023, 15, 3325−3335

Read Online

ACCESS | Metrics & More | Article Recommendations | Supporting Information



**ABSTRACT:** Aerosol jet printing is a noncontact, digital, additive manufacturing technique compatible with a wide variety of functional materials. Although promising, development of new materials and devices using this technique remains hindered by limited rational ink formulation, with most recent studies focused on device demonstration rather than foundational process science. In the present work, a systematic approach to formulating a polymer-stabilized graphene ink is reported, which considers the effect of solvent composition on dispersion, rheology, wetting, drying, and phase separation characteristics that drive process outcomes. It was found that a four-component solvent mixture composed of isobutyl acetate, diglyme, dihydrolevoglucosenone, and glycerol supported efficient ink atomization and controlled in-line drying to reduce overspray and wetting instabilities while maintaining high resolution and electrical conductivity, thus overcoming a trade-off in deposition rate and resolution common to aerosol jet printing. Biochemical sensors were printed for amperometric detection of the pesticide parathion, exhibiting a detection limit of 732 nM and a sensitivity of 34 nA $\mu M^{-1}$, demonstrating the viability of this graphene ink for fabricating functional electronic devices.

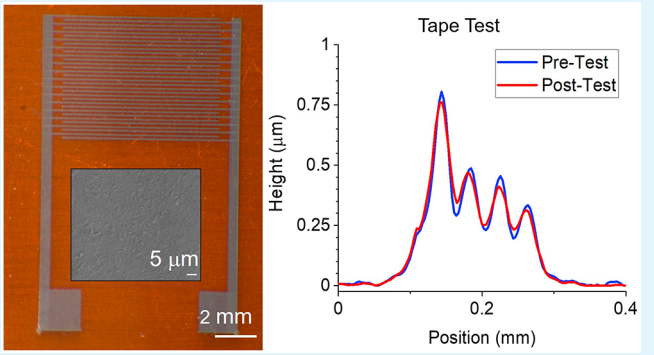


**KEYWORDS:** *printed electronics, nanomaterial ink, 2D materials, electrochemical sensing, flexible electronics*

## INTRODUCTION

A new generation of electronics will include conformal, flexible, and stretchable devices, such as electronic skin,[1] mechanical sensors,[2] energy harvesting and storage devices,[3,4] biomedical[5] and biological sensors,[6−8] and wireless antennas.[9] Printing technologies provide a compelling fabrication platform for these systems, with inherent advantages for large-area and flexible form factors.[10] Roll-to-roll methods such as gravure printing support high-throughput and low-cost manufacturing,[11,12] while digital methods such as inkjet and aerosol jet printing (AJP) streamline prototyping and customization by reducing cost and time required to generate new printing patterns via software. In recent years, hybrid electronics possessing material versatility, mechanical compliance, and large-area printability have emerged as an important complement to the high computing performance and capabilities of silicon devices.[13] To support these advances, printing methods rely on liquid-phase inks tailored to specific deposition methods to pattern functional materials with precision and reliability. Understanding how physicochemical properties of the inks couple with the physical mechanisms of specific printing processes is crucial for streamlining materials integration in printed electronics.

During device prototyping, designs are continuously optimized and new materials are introduced to provide distinct functionality. AJP is particularly compelling in this context due to its noncontact, additive, and digital nature. During AJP, an ink is pneumatically or ultrasonically atomized into aerosol droplets of micrometer size, which are then transported on a carrier gas stream into a deposition nozzle.[14] There, the aerosol stream is constricted by a sheath gas and directed to a substrate, allowing patterning with ∼10−100 $\mu$m resolution.[14] These operational properties give AJP an advantage over other additive manufacturing techniques provided functional inks can be designed with the appropriate fluid viscosity, particle size, and stability needed for the atomization process and subsequent printing. Validating this broad materials compatibility, dispersions or solutions of metals,[15] ceramics,[16] polymers,[17] and small molecules have been formulated into inks and printed with this method.

**Received:** October 21, 2022
**Accepted:** December 21, 2022
**Published:** January 6, 2023

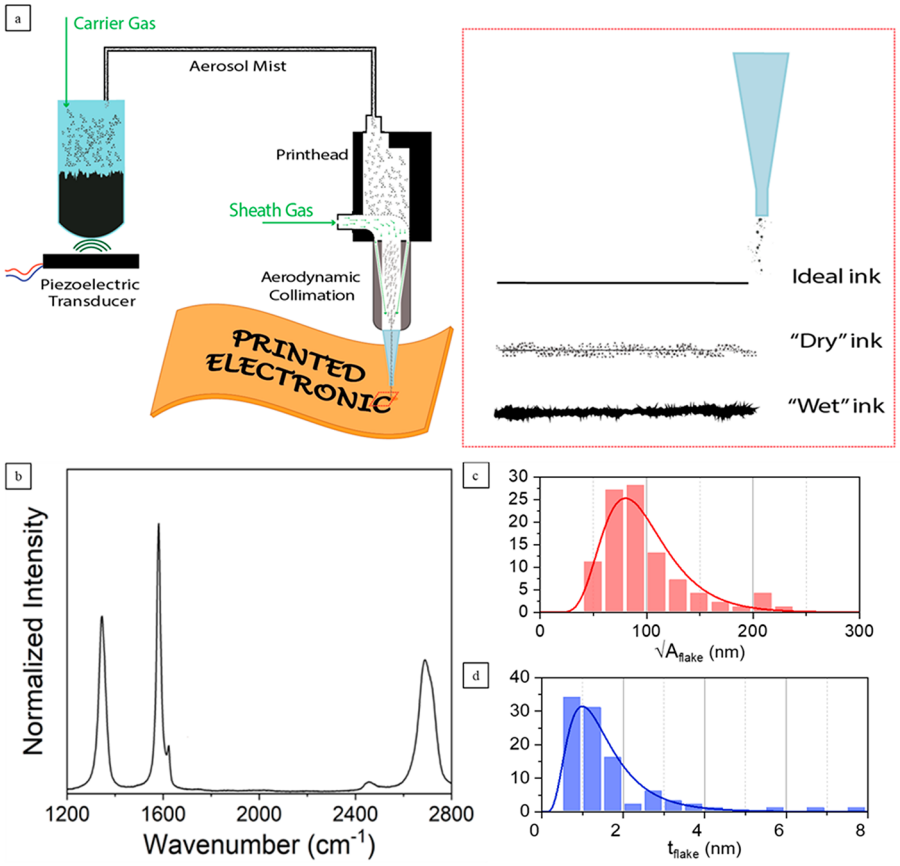


**Figure 1.** (a) Schematic of the AJP process, in which an ink is ultrasonically atomized and pneumatically transported to a printhead on a carrier gas. A sheath gas prevents droplet impingement on the printhead interior and focuses and accelerates the aerosol stream through a deposition nozzle and onto a substrate. Inset depicts three possible print results based on ink formulation: first, an ideal ink allows printing of high aspect-ratio features with consistent resolution and negligible overspray; a "dry" ink formulation results in overspray due to excessive evaporation in the aerosol state; a "wet" ink results in profiles lacking constant resolution and irregular edges due to liquid spreading on the surface of the substrate. (b) Normalized Raman spectrum of thermally treated graphene powders, where G, D, D′, and 2D peaks are clearly resolved. (c) Graphene flake lateral size distribution histogram, which follows a log-normal distribution with a mean of 97.89 ± 4.07 nm, and (d) thickness distribution histogram, which also follows a log-normal distribution with a mean of 1.59 ± 0.12 nm. Both distributions were obtained from AFM measurements.

Provided an ink can be atomized, it is relatively straightforward to achieve basic deposition. As a result, many studies focus on narrowly optimizing processing parameters for a given ink, such as carrier and sheath gas flow rates, and move onto device demonstration without considering broader consequences of the ink composition. Fewer studies take a step back to consider optimization of the ink itself, a more complex problem with broader potential to generally improve process outcomes and establish foundational understanding of ink-process interactions.

In the present work, a graphene ink is designed considering the specific physical and chemical properties required for AJP. Graphene has been selected for this study due to its electrical conductivity and biocompatibility as well as mechanical and electrochemical stability,[12,18,19] which make it a desirable material in biosensing applications such as detection of COVID-19 antigens or S1 proteins,[20] as well as smaller molecules such as histamines for food safety[21] or cytokines for disease monitoring.[22] Herein, the systematic formulation of a suitable graphene ink considers mechanistically relevant physicochemical properties, such as atomization properties under ultrasonic perturbation,[23,24] drying properties during pneumatic manipulation,[25,26] and microstructure of the graphene patterns following deposition and curing. The utility of the resulting ink formulation is then demonstrated by printing electrochemical sensors on flexible polyimide substrates for amperometric detection of the pesticide parathion given its environmental impact and human toxicity.[27,28] This work thus demonstrates the applicability of this specific graphene ink for biosensors while providing additional insight into ink formulation to accelerate the broader development of AJP for new materials[29] and devices.[30]

## MATERIALS AND METHODS

**Materials.** Isobutyl acetate (IBA), diglyme (Dig), dihydrolevoglucosenone (commercialized as Cyrene, Cyr), ethyl cellulose (EC, 4 cP grade), graphite, acetylcholinesterase (AChE) from *Electrophorus electricus* (lyophilized powder, 200−1000 units/mg), and parathion were purchased from Millipore Sigma (St. Louis, MO, USA). Nitrocellulose (NC, catalog no. 712) was purchased from Scientific Polymer Products (Ontario, NY). Glycerol (Gly) and 200-proof ethanol were obtained from Fisher Scientific (Waltham, MA). Ag/AgCl paste (Cl-4001) was purchased from Electron Microscopy Sciences (Hatfield, PA, USA). All materials were used as received without further purification.

**Ink Preparation.** Graphene powder with ethyl cellulose (EC) was prepared following the procedure described previously.[31] Briefly, 1% w/v EC was dissolved in 20 L of ethanol, 6 kg of graphite was added, and the resulting mixture was processed for 96 h at 3500 rpm in a continuous-flow inline shear mixer setup (Silverson Machines 200L).


https://doi.org/10.1021/acsami.2c18838
ACS Appl. Mater. Interfaces 2023, 15, 3325−3335

The resulting suspension was centrifuged with a *g*-force of ∼8100*g* for 30 min; the supernatant was collected and flocculated by combining at 1.74:1 w/w with a 0.04 g $mL^{-1}$ NaCl solution, followed by centrifugation at ∼9380*g* for 7 min. The generated supernatant was discarded, and the remaining products were rinsed with DI water and collected by vacuum filtration before being dried under an IR lamp. The process yielded a powder containing 30 wt % graphene.

All inks were prepared with the aforementioned 10 mg $mL^{-1}$ of EC-coated graphene, 5 mg $mL^{-1}$ of NC, 80 vol % of primary solvents (IBA, Dig, or 1:1 IBA/Dig), and 20 vol % of low-volatility cosolvent (Cyr or 1:1 Cyr/Gly). After combining the chemicals, the inks contained in 20 mL scintillation vials were agitated overnight in an ultrasonic bath prior to printing.

**Instrumentation.** For printing experiments, a custom-built aerosol jet printer was used with 200 $\mu$m tapered plastic nozzle tips for typical experiments (Nordson, Westlake, OH, USA). Dynamic light scattering (DLS) measurements were performed with a Malvern Zetasizer Nano ZS (Malvern Panalytical, Malvern, United Kingdom). Optical profilometry was performed with a Zygo 7100 optical surface profiler (Zygo, Middlefield, CT, USA, *z* resolution 0.1 nm and optical resolution 2.9 $\mu$m), and the corresponding data were processed with Gwyddion and analyzed with a MATLAB script. Rheology measurements were obtained with an AR2000EX rheometer (Thermal Advantage, Phoenix, AZ, USA, with torque and displacement resolution of 1 mN·m and 40 nrad, respectively) equipped with a Peltier plate for temperature control. Scanning electron microscopy (SEM) was performed using a FEI Quanta 250 FE-SEM (FEI Company, Hillsboro, OR, U.S.). Microscopy images were obtained with a Motic Panthera Tec (Motic, Schertz, TX, USA), and resistance was measured with a four-point probe configuration using a Keithley 2450 source measure unit (Keithley, Cleveland, OH, USA, with 0.012% measure accuracy). Electrochemical characterization experiments were performed with a CH Instruments 600E series potentiostat (CH Instruments Inc., Bee Cave, TX, USA, with resolution <1 pA) and a PalmSens4 impedance analyzer (PalmSens BV, Houten, The Netherlands, with potential and current resolution <0.1% and <0.02%, respectively). Atomic force microscopy (AFM) data were obtained using an Asylum Cypher microscope (Oxford Instruments, Abingdon, Oxfordshire, U.K.), and Raman spectroscopy was performed with a LabRAM HR Evolution microscope with a 532 nm laser operating at 10% power (Horiba, Irvine, CA, USA). AFM data were processed with Gwyddion and analyzed with a MATLAB script to count individual flakes using an edge approximation algorithm.

**Graphene Characterization.** Prior to AFM measurements, EC-coated graphene powders were redispersed in ethanol to obtain a 2% w/v solution and then diluted 200 times. This dispersion was drop-casted on a 300 nm thermally grown $Si/SiO_2$ chip previously treated with 2.5 mM solution of 3-aminopropyl triethoxysilane in isopropanol for 10 min. The sample was then thermally treated at 350 °C for 30 min in air to remove both EC and silane prior to scanning. AFM analysis was performed in AC air/tapping mode with a set point of 700 mV and a scan rate of 1 Hz over a 5 $\mu$m × 5 $\mu$m area. The phase angle was 50−51°.

Raman spectroscopy was performed after redispersing EC-coated graphene powders in a 90:10 v/v solution of ethanol and ethyl lactate that was filtered with 1.6 $\mu$m glass microfiber syringe filter (Whatman). The resulting solution was spin coated five times onto plasma-treated glass substrates at 2000 rpm. Lastly, the sample was thermally annealed at 350 °C in order to remove the polymer. Raman characterization was performed three times with an acquisition time of 30 s using a laser spot size of 1 $\mu$m and a 2400 g/mm grating.

**Image Processing.** Optical microscopy images were processed by first applying a median filter to remove noise, followed by a Laplacian of Gaussian filter along the *y* direction to detect feature edges. Finally, a Hough transform was performed to rotate the lines to horizontal and find their average distance along the *y* direction, which corresponds to the line resolution.

## RESULTS AND DISCUSSION

To formulate a graphene ink suitable for AJP (Figure 1a), this work follows a series of steps including material selection, solvent composition tuning, print calibration and optimization, and characterization of print outcomes (resolution, deposition rate, line quality) and functional properties (electrical conductivity, adhesion).

**Materials Selection and Characterization.** Graphene inks containing the EC polymer as a dispersant have shown considerable promise for printed electronics, including formulations tailored to inkjet,[31] gravure,[11,12] flexographic,[32] and screen printing.[33] Following this previous work, graphene was prepared by liquid-phase exfoliation in an ethanol-based solution of EC. Raman spectroscopy was performed to assess the quality of graphene and defects associated with the exfoliation process (Figure 1b). While the Raman spectrum may vary following mixing with NC, printing, and annealing,[21,22] residue from the NC would convolute interpretation of measurements following printing,[34] so for a cleaner evaluation of the graphene flakes this measurement is done for films prepared from the raw Gr powder as-prepared with EC, following annealing. The D-to-G peak intensity ratio ($I_D/I_G$) provides a metric for graphene quality, as these peaks are respectively associated with phonon scattering and the graphitic peak stemming from the relative motion of $sp^2$ carbon atoms.[35] The $I_D/I_G$ ratio was observed to be ∼0.65, higher than standard surfactant-supported graphene but lower than that for reduced graphene oxide and other similar graphene size distributions.[36] This value indicates that some defects were introduced during either annealing or exfoliation. The D′ peak is commonly associated with the second order of the intravalley D peak and the 2D peak stemming from the D′ overtone.[37] The G, D, D′, and 2D peaks are present at ∼1350, ∼1580, ∼1620, and ∼2700 $cm^{-1}$, respectively, consistent with other reports of spin-coated, few-layered graphene samples.[38] The position of the G peak and the ratio between the G and 2D peaks ($I_G/I_{2D}$) serve as indicators of the number of graphene layers. As the number of layers increases, the 2D band will broaden and upshift with respect to single layer graphene.[38] Therefore, the position of the G-peak at ∼1580 $cm^{-1}$ demonstrates a film composed of few-layered graphene flakes, further substantiated with the characteristic $I_G/I_{2D}$ ratio of ∼1.96, close to that of mechanically exfoliated few-layer graphene.[39] The analysis of a population of 50−100 graphene flakes by AFM revealed the presence of graphene nanosheets with a mean lateral size of 97.89 ± 4.07 nm and mean thickness of 1.59 ± 0.12 nm, dimensions consistent with previous reports of EC-stabilized graphene[31,40] and shear-mixed graphene nanosheets (Figure 1c,d).[41]

While EC provides a suitable dispersant for the production of graphene, nitrocellulose (NC) has previously been demonstrated as an alternative dispersant yielding superior mechanical properties.[34] In that earlier study, improved adhesion and cohesion of graphene films were attributed to the presence of NC decomposition residue acting as a mechanical binder. Therefore, in this work NC was included as an additive in the ink formulation stage to provide this benefit. Importantly, this obviates the use of large quantities of this material for graphene exfoliation, for which the hazardous nature of NC is a barrier to industrial adoption, while still maintaining the advantages of NC. The addition of NC provides an additional constraint for ink formulation,


https://doi.org/10.1021/acsami.2c18838
ACS Appl. Mater. Interfaces 2023, 15, 3325−3335

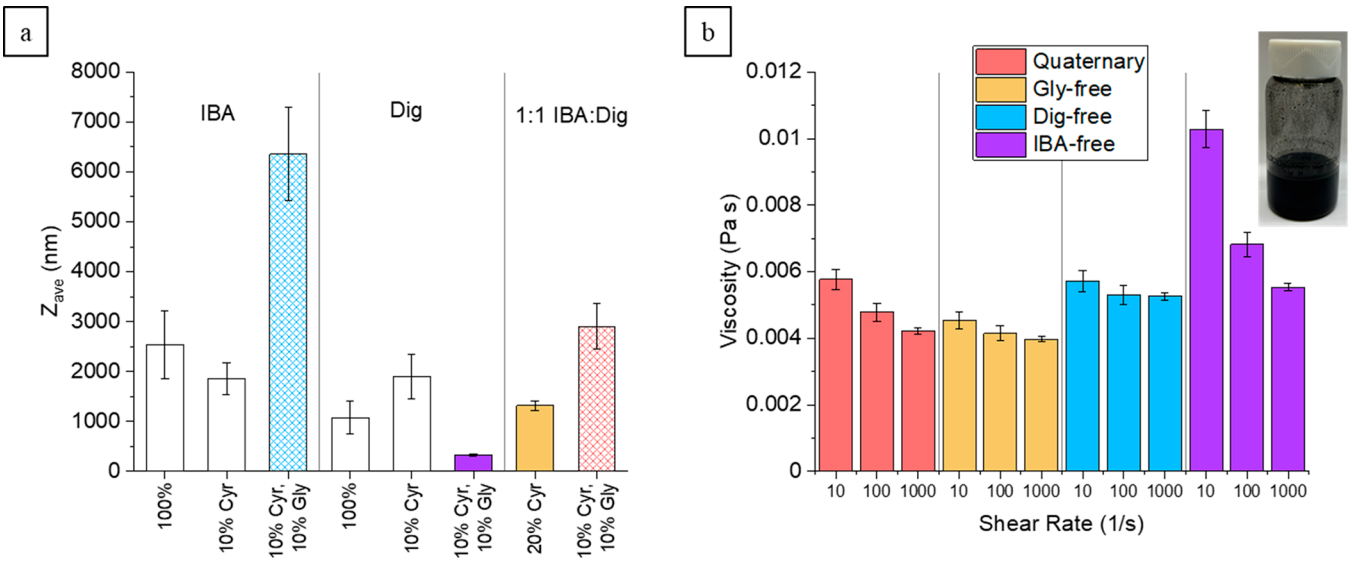


**Figure 2.** (a) DLS measurements of the hydrodynamic diameter of EC dispersed in different model solvent mixtures. White columns are reference solutions not used for printing, while colored columns represent solvent systems used in printing experiments; solid coloring indicates fully dissolved EC, hatched columns indicate mixtures for which the EC solution becomes turbid. (b) Viscosity of the four candidate inks, with inset image showing a vial of the final ink.

**Table 1. Chemical Compositions of the Inks Formulated for AJP**

| ink formulation | EC-graphene (mg mL$^{-1}$) | nitrocellulose (mg mL$^{-1}$) | glycerol (vol %) | Cyrene (vol %) | isobutyl acetate (vol %) | diglyme (vol %) |
|---|---|---|---|---|---|---|
| quaternary | 10 | 5 | 10 | 10 | 40 | 40 |
| Gly-free | 10 | 5 | | 20 | 40 | 40 |
| Dig-free | 10 | 5 | 10 | 10 | 80 | |
| IBA-Free | 10 | 5 | 10 | 10 | | 80 |

narrowing the scope of solvents with suitable chemical properties.

**Solvent Selection and Polymer Conformation.** The next step in ink formulation was the selection of candidate solvents based on physicochemical properties, such as molecular weight,[25] viscosity, boiling point, vapor pressure,[42,43] and surface tension,[43,44] as well as chemical compatibility with the EC-coated graphene and NC additive. Micrometer-scale droplets such as those used in AJP exhibit evaporation time scales on the order of milliseconds. Thus, the drying behavior of all formulated inks is of particular concern: excessive or insufficient drying would exacerbate overspray or unstable substrate wetting, respectively, necessitating a careful balance achieved by tailoring the solvent composition and volatility. Considering their ability to disperse EC-coated graphene and dissolve NC, isobutyl acetate (IBA) and diglyme (Dig) were selected as the two principal candidates making up the solvent system needed for ink formulation. These solvents also feature disparate vapor pressures of 1730 and 427 Pa for IBA and Dig, respectively, to tailor evaporation characteristics.[25,26] In addition, theoretical aspects of vapor transport phenomena reported by Feng[25] suggest the inclusion of low vapor pressure cosolvents. Cyrene (Cyr) has been shown to be an excellent graphene solvent,[45,46] and glycerol (Gly) was considered given its ability to cause gelation of EC-coated graphene powders, as shown in previous studies,[47] while also having lower surface tension than Cyrene (Supporting Information Table S1). All four solvents are miscible, but the polymers are immiscible in pure glycerol. This supports a stable system prior to printing, but during deposition the glycerol evaporates at the slowest rate and therefore is enriched and drives the system into phase inversion.[47] Examples of printed features obtained with inks formulated with different, simpler solvent systems are shown in Figure S1. The lack of control over the dynamic composition of the ink droplets between atomization, pneumatic manipulation, and substrate impingement leads to excessive droplet drying for unitary (Figure S1a,b) solvent systems and graphene traces lacking lateral cohesion and showing significant overspray. Inks formulated with binary and ternary solvent systems (Figure S1c–f) show varying degrees of lateral cohesion, overspray, and porosity, showing how control of the chemical composition of the droplets upon impingement is fundamental to ensure high quality prints.[48]

Following selection of candidate solvents, DLS was performed on model solutions of the dispersant EC in various solvent mixtures to evaluate solvent effects on polymer conformation. As shown in Figure 2a, in the combination of IBA, Cyr, and Gly, EC is not homogeneously dissolved and forms a visibly turbid dispersion. Conversely, the combination of Dig, Cyr, and Gly does not lead to turbidity, which is reflected in the hydrodynamic diameter ($Z_{ave}$) values reported in Figure 2a. A 1:1 mixture of the two primary solvents IBA and Dig combined with only Cyr or a combination of Cyr and Gly yielded intermediate values of $Z_{ave}$, with destabilization and subsequent phase separation of the EC-rich regions observed upon the addition of Gly (Figure S2). The various dispersion stabilities motivated further study of four different ink formulations, outlined in Table 1. These four inks are identified herein as the quaternary ink (containing all four solvents), and three inks are identified based on the component they lack (IBA-free, Dig-free, and Gly-free). A Cyr-free ink was not considered, as 20% Gly did not support


https://doi.org/10.1021/acsami.2c18838
ACS Appl. Mater. Interfaces 2023, 15, 3325−3335

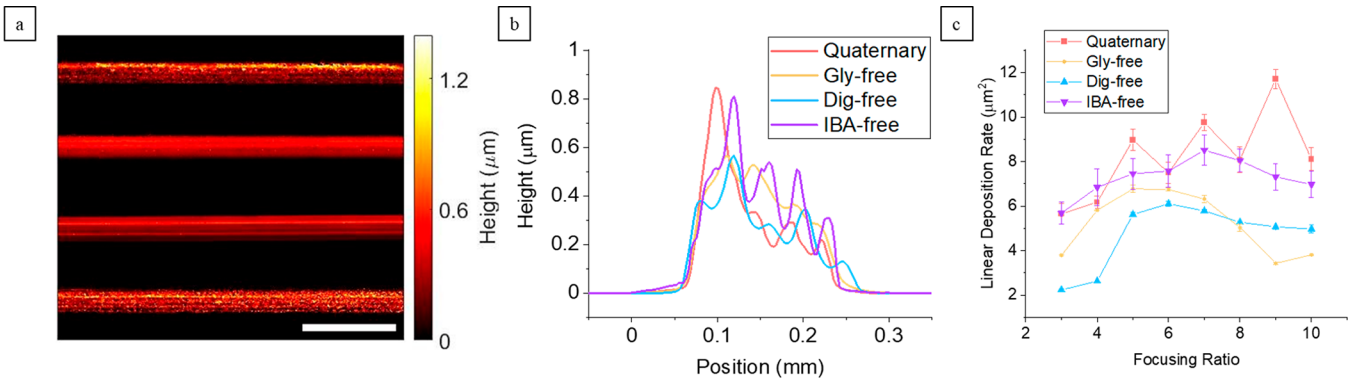


**Figure 3.** (a) Representative optical profilometry for samples obtained with the four ink formulations for a focusing ratio of 5, printed on a glass substrate. From top to bottom, traces obtained with quaternary, Gly-free, Dig-free, and IBA-free ink formulation printed at 35, 40, 43, and 43 V are shown, respectively (scale bar: 0.5 mm). (b) Line plot showing averaged cross sections for representative prints, with their profiles shown individually in Figure S3 including standard deviation. (c) Measured linear deposition rates for focusing ratios of 3−10.

stable dispersion of the graphene. For consistency, all of the formulations contained 10 mg $mL^{-1}$ of EC-coated graphene and 5 mg $mL^{-1}$ of the adhesion promoter nitrocellulose[34] and exhibited uniform dispersions with negligible sedimentation at room temperature (Figure 2b, inset). Because the primary purpose of this work is to illustrate the role of each solvent, finer variations of solvent and cosolvent ratios were not considered. Such detailed optimization could certainly be done to tailor properties but would require an explicit application-specific figure of merit.

Because viscosity is a key determinant of atomization during AJP, the viscosity of the four inks was measured with a shear rheometer (Figure 2b). Although all formulations exhibit viscosities with similar trends to the theoretical values estimated for the solvents alone (Supporting Information, Table S2),[49,50] the interaction of solvents with nonvolatile components of the ink impacts the rheological characteristics. The quaternary formulation shows a more pronounced shear thinning behavior than the ink formulated without glycerol, yet they have comparable viscosities in the measured range of shear rates, especially at higher shear rates. These observations show that even though the protic additive has a viscosity almost 2 orders of magnitude higher than Cyrene (Table S1), the conformational change of EC chains plays an important role in determining the final viscosity and shear thinning behavior of the inks. The formulations with a single primary solvent show remarkably different viscosities as well as shear thinning. The Dig-free formulation has 80 vol % of IBA, which destabilizes EC and reduces shear thinning. Conversely, in the IBA-free formulation, the polymer chains of the cellulose derivative are free to entangle and establish a high number of interchain secondary bonds, which is reflected in a higher viscosity at low shear rates and more pronounced shear thinning behavior.

**Printing Process and Characterization.** With viscosity values of all inks in a suitable range for ultrasonic atomization,[14] printing experiments were performed. To determine a suitable atomization voltage for the four different inks, the carrier gas flow rate was maintained at 10 sccm and the voltage was gradually increased until printing began, as determined manually using a process camera. Because of its singular primary direct role in setting an aerosol volume fraction, the atomizer voltage was first varied to establish a suitable deposition rate that resulted in visible deposition. Modulating the atomizer voltage is expected to shift the print output by varying the deposition rate, without altering the gas flow field. Thus, comparable deposition rate for the four different inks was targeted rather than a broad sweep of voltage that would push deposition conditions further from practical printing parameters. The lowest atomizer voltages that allowed for consistent printing were 35 V for the quaternary ink, 40 V for the Gly-free ink, and 43 V for both inks with a single primary solvent ("Dig-free" and "IBA-free"). The lowest atomization voltages that allowed for consistent and dense deposition were chosen to minimize heating of the ink sample and avoid potential sonochemical reactions, and resulting prints were thermally treated at 70 °C for 10 min to remove excess solvent and then cured at 325 °C for 30 min to decompose the polymer dispersants and improve electrical conductivity before cooling naturally. Patterns printed with a sheath:carrier gas flow rate ratio (also known as the focusing ratio) from 3 to 10 were analyzed by optical profilometry (Figure 3a) to determine the postprocessed deposition rate based on the sample cross-sectional area. A primary metric of interest is the linear deposition rate (or speed-normalized deposition rate, Figure 3b and Figure 3c, respectively), which is dimensionally equivalent to the cross-sectional area of a single printed trace and accounts for speed-dependent effects such as liquid spreading following deposition.[51] With the above-mentioned atomizer settings, it is possible to obtain patterns with comparable cross-sectional areas and, consequently, deposition rates, which allow for a meaningful comparison of the properties of sintered prints. In Figure 3a, optical profilometry data of narrow bar prints (10 passes offset) with a focusing ratio of 5 exhibit distinct morphology caused by the different ink formulations. The toolpath used for the reported prints is schematically shown in Figure S3e and contains an offset between adjacent lines and inherent asymmetry leading to the final nonuniform structure. Dig introduces more long-range roughness in the final structure when acting as the sole primary solvent (Figure 3a, fourth print), likely due to its higher boiling point with respect to IBA that allows for Gly to cause phase inversion.[47] IBA yields a more uniform three-dimensional profile (Figure 3a, third print), as the fast drying, including in the aerosol state, could prevent ordering during phase inversion as extensively as observed for Dig. For the IBA-Dig primary solvent mixture, the effect of glycerol on the morphology can also be analyzed. The inclusion of the low-vapor pressure, high-viscosity, protic solvent produces features with higher surface roughness (Figure 3a, first print) compared


https://doi.org/10.1021/acsami.2c18838
ACS Appl. Mater. Interfaces 2023, 15, 3325−3335

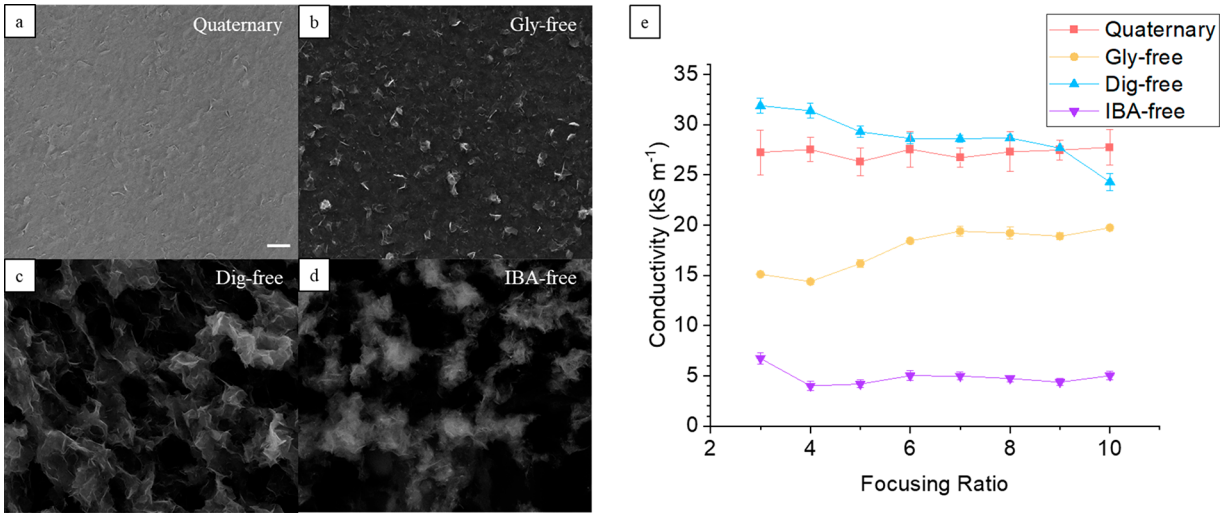


**Figure 4.** SEM micrographs of the morphology of the (a) quaternary, (b) Gly-free, (c) Dig-free, and (d) IBA-free samples on silicon wafers (scale bar: 5 $\mu$m for all). (e) Electrical conductivity for the four ink formulations printed with focusing ratios of 3−10.

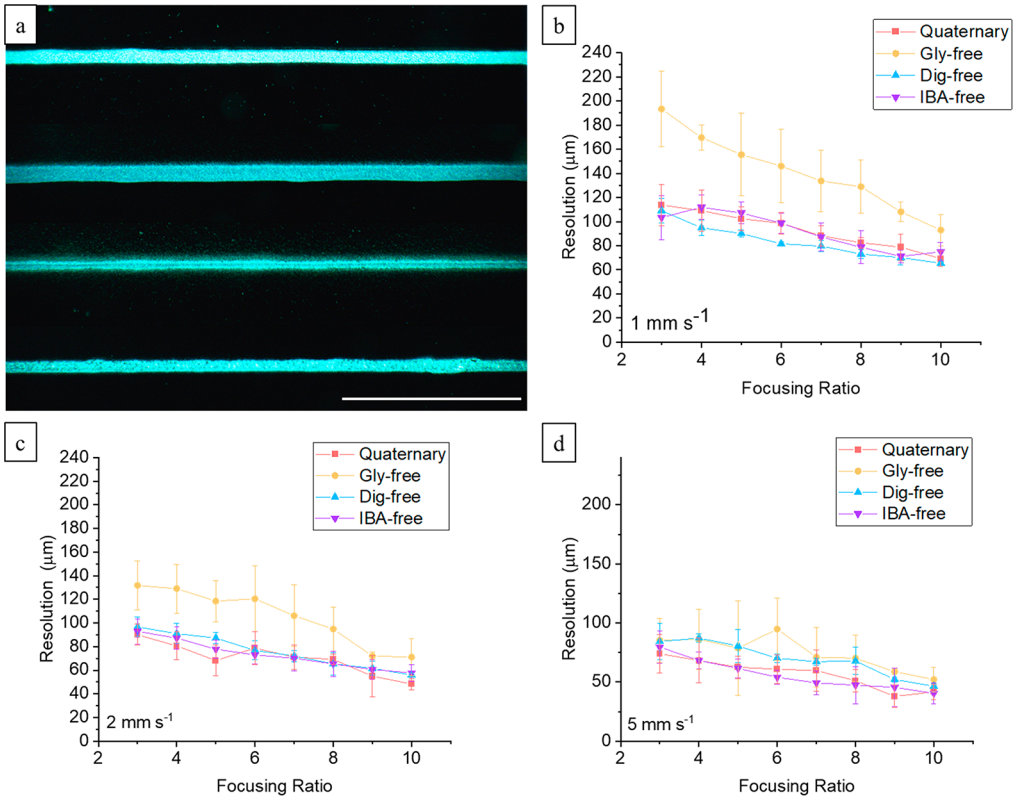


**Figure 5.** (a) Dark field optical microscopy images of lines printed on glass with a single pass at 1 mm $s^{-1}$ and focusing ratio of 5 using a 200 $\mu$m nozzle tip with the quaternary, Gly-free, Dig-free, and IBA-free ink formulations shown from top to bottom, respectively (scale bar: 1 mm). Line resolution results for the four ink formulations at feed rates of (b) 1, (c) 2, and (d) 5 mm $s^{-1}$.

to that containing only Cyr as a cosolvent (Figure 3a, second print). Notably, the inclusion of Gly allows consistent printing with an atomization voltage of 35 V, 5 V below the threshold without Gly. This observation is attributed to the coiling of EC, which removes the entanglement effects of the polymer chains and allows for sustained atomization at lower voltage, an effect absent in the ink prepared with 20 vol % of Cyr.

The microstructure resulting from the different ink formulations was assessed by scanning electron microscopy for samples deposited on silicon wafers. The inks formulated with 40 vol % of IBA and Dig lead to a dense and uniform surface microstructure (Figure 4a,b), whereas patterns obtained with 80 vol % of either IBA or Dig lead to more porous prints (Figure 4c,d). To understand how this morphology impacts functional properties, four-point probe electrical measurements were conducted to evaluate the electrical resistivity. As shown in Figure 4e, the quaternary and Dig-free inks have the highest conductivities, ranging from 27.5 to 32.5 kS $m^{-1}$, which are higher than those previously reported for devices printed with the same EC-coated



https://doi.org/10.1021/acsami.2c18838
ACS Appl. Mater. Interfaces 2023, 15, 3325−3335

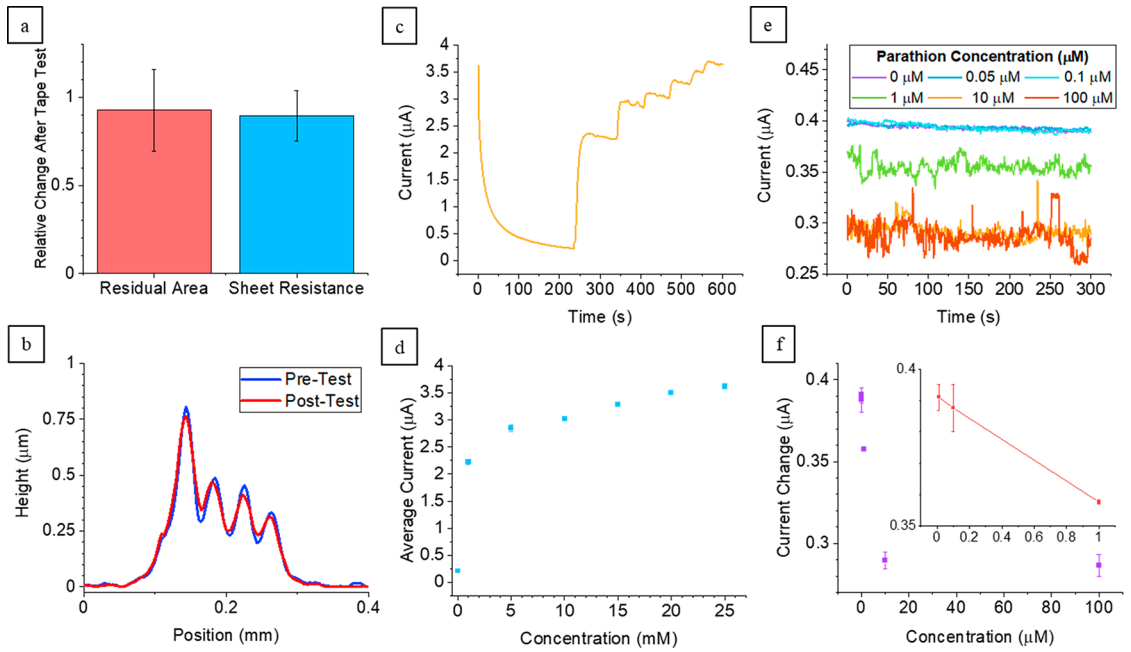


**Figure 6.** (a) Relative cross-sectional area and sheet resistance after testing graphene patterns for adhesion on Kapton substrates. (b) Cross-sectional profile comparison of a sample before and after tape test, where the retention of fine features can be observed. (c) Electrochemical response of a graphene amperometric sensor printed on Kapton to the addition of ATCC and (d) its calibration curve. (e) Time response of amperometric sensors to the addition of increasing amounts of the pesticide parathion. (f) Average electrochemical response to parathion, used as a calibration curve. Inset shows the linear range of the electrochemical response, which lies between 0.01 and 1 $\mu$M.

graphene powders and glycerol though extrusion printing.[47] The Gly-free ink resulted in intermediate conductivities of 15−20 kS m$^{-1}$, and Dig as the only primary solvent yielded the lowest electrical conductivity, with an average of ∼5 kS m$^{-1}$, on par with that observed for inks exhibiting significant phase inversion.[47]

For high resolution patterning, the width of a single printed line in the $x$−$y$ plane imposes a limit on precision. This precision limit was evaluated by optical microscopy, with representative images for each ink shown in Figure 5a. Because liquid spreading effects impart sensitivity in resolution to print speed, patterns with single line features printed with feed rates of 1, 2, and 5 mm s$^{-1}$ were analyzed (Figure 5b−d). Notably, the Gly-free formulation shows a different behavior from the Gly-containing inks, especially at lower feed rates (Figure 5b,c), which suggests that the presence of the protic, low-volatility cosolvent reduces in-plane spreading of the liquid, eventually leading to a modest speed-invariance for the resolution.[47] The Gly-free ink is sensitive to the manufacturing feed rate, as liquid spreading at high linear deposition rate increases the printed line width. This phenomenon is typical behavior for AJP and results in a trade-off between deposition rate and resolution. The Gly-containing inks circumvent this limitation by exploiting the effect of Gly on dispersion stability. In the aerosol phase and following deposition, the shift in solvent composition to a Gly-rich state leads to destabilization of the dispersed solids and corresponding formation of a colloidal gel-like structure. The graphene thus remains more localized to where it was deposited. The profilometry data from Figure 3a,b further support this, with topographical features evident for the quaternary ink during multipass printing. Single-pass printed lines also show considerable deposition rates, with lines as thick as 600 nm printed at 1 mm s$^{-1}$ while maintaining appreciable resolution values (Figure S4). When using a nozzle tip with an orifice of 200 $\mu$m diameter and printing with a focusing ratio of 10, the finest resolutions were found to be 65, 48, and 40 $\mu$m with feed rates of 1, 2, and 5 mm s$^{-1}$, respectively. Additionally, the effect of each primary solvent could be observed, with Dig leading to less regular line edges (Figure 5a, fourth line from the top) and IBA leading to significant overspray, which reduces the overall line quality (Figure 5a, third line from the top). An intermediate line morphology was observed for the prints obtained with the quaternary ink (Figure 5a, first line from the top), exhibiting smoother line edges and reduced overspray. Additional experiments were performed using a 150 $\mu$m nozzle, with feed rates of 1, 2, and 5 mm s$^{-1}$ corresponding to resolutions of 30, 28, and 21 $\mu$m, respectively (Figure S5).

**Ink Analysis and Device Demonstration.** To summarize the data collected for all four formulations, the quaternary ink can be printed at the highest deposition rate with the lowest atomization voltage of 35 V out of the formulations studied, has a continuous and dense microstructure after curing, one of the highest conductivities with an average value of ∼27.5 kS m$^{-1}$, uniform line-edge morphology, and consistently high line resolution. The Gly-free ink shows uniform microstructure but is hindered by intermediate conductivity, and the achievable resolution is particularly sensitive to the print speed selected for fabrication (Figure 5b−d, orange plot). The ink prepared with only IBA as a primary solvent exhibits high conductivity, porous surface structure (Figure 4c), and good core line resolution (Figure 5b−d) but is hindered by significant overspray (Figure 5a, third line), which is problematic for multimaterial and high-density electronics. Lastly, the ink formulated with Dig as the only primary solvent exhibits the lowest conductivity of ∼5 kS m$^{-1}$ (Figure 4e), high porosity (Figure 4d), and poor line edge smoothness (Figure 5a, fourth line). Considering all these results, the quaternary ink was


https://doi.org/10.1021/acsami.2c18838
ACS Appl. Mater. Interfaces 2023, 15, 3325−3335

chosen as the formulation most suitable for AJP and was therefore used for subsequent studies.

In this study, NC was used as an additive to promote mechanical cohesion of the printed graphene based on prior work.[34] Importantly, while the prior study used NC as the sole dispersant for graphene, the reactive nature of NC imposes constraints on scalable production. By using EC for graphene production and subsequently adding a small amount of NC during ink formulation, the benefits of each polymer dispersant can be maintained. To confirm that NC remains effective in this process flow, samples were printed with the quaternary ink on polyimide and cured to assess adhesion properties. The cross-sectional area and sheet resistance were measured before and after tape tests to evaluate changes in the material properties (Figure 6a,b and Figure S6). Results collected from a population of 20 prints showed that ∼93% of the original cross-sectional area is maintained in all samples and the prints experience a decrease in sheet resistance of ∼10%, similar to previously reported studies where NC was shown to enhance mechanical properties of graphene based patterns.[34] The decrease in both cross-sectional area and sheet resistance suggests that some porosity is removed during the tape test.[52]

To demonstrate the functionality of this graphene ink, amperometric sensors were fabricated on Kapton using a dipstick geometry for pesticide sensing. Prior to sensing, silver paste was deposited on the sensor contact to mitigate wear from the potentiostat clip, and acrylic polish was used to passivate the area between the contact and the working sensor area, which has a diameter of 3 mm. After passivation, enzymatic functionalization was performed on the working area with 10 $\mu$L of a solution formed in equal volumetric parts of 20 units/mL of AChE and 0.25% glutaraldehyde. Each device was stored at 4 °C overnight prior to use. Electrochemical tests were performed in PBS (phosphate buffer saline) at a pH of 7.4 using an electrochemical cell consisting of the AJP graphene working electrode, a commercial platinum wire as the counter electrode, and a commercial Ag/AgCl (1 M) electrode as the reference. The electrochemical enzymatic activity was tested by adding increasingly concentrated aliquots of acetylthiocholine chloride (ATCC) to the electrochemical cell. As AChE catalyzes the oxidation of ATCC, an electrochemical signal is measured (Figure 6c). Such oxidation occurs at +0.4 V vs Ag/AgCl as noted in previous studies.[53]

With the present sensors, ATCC becomes saturated near 10 mM, a concentration that was used throughout the rest of the studies (Figure 6d). Subsequently, sensors were incubated for 10 min in parathion, rinsed in PBS, and amperometric activity was recorded in 10 mM of ATCC. As the pesticide irreversibly bound to AChE, active sites of the enzyme became sterically blocked, which restricted ATCC oxidation; thus, with fewer catalytic sites available for oxidation, the amperometric signal decreased due to successive incubation in parathion (Figure 6e). The sensor was calibrated at parathion concentrations between 50 nM and 1 mM, displaying a linear range from 10 nM to 1 $\mu$M, a sensitivity of 34 nA $\mu M^{-1}$, and a detection limit of 732 nM (Figure 6f). Hence, these results demonstrate that the developed sensor could be used in label-free monitoring of trace amounts of pesticides in food and water samples.[54] Moreover, this graphene ink can be used to fabricate interdigitated microelectrodes arrays (i.e., electrodes that typically display high signal-to-noise ratios, low capacitive charging, and low detection limits during sensing)[55] with high resolution (finger comb width and pitch of ∼65 and 200 $\mu$m, respectively) and thickness of ∼700 nm (Figure S7). The combination of this graphene ink and AJP fabrication could hence provide a promising platform for future sensor development where high sensitivity and label-free monitoring are crucial for in-field environmental monitoring or clinical diagnostics.

## CONCLUSIONS

In the present work, a systematic approach to the formulation for a graphene ink for aerosol jet printing has been shown. In contrast to a previously demonstrated ink,[34] the inclusion of the additive nitrocellulose during ink preparation does not compromise the scalable production of EC-coated graphene while maintaining the high mechanical performance of the cured graphene patterns. The introduction of NC in the ink formulation step was made possible by selecting a quaternary solvent mixture in which the additive can be dispersed while maintaining compatibility with the printing constraints, which include high atomization rate, droplet drying during pneumatic manipulation, and substrate wetting following deposition.

Formulations containing a mixture of primary solvents with different physicochemical properties supported control over the drying behavior of the ink upon pneumatic manipulation and deposition, leading to graphene patterns with uniform microscale morphology. Additionally, the inclusion of the high viscosity cosolvent glycerol circumvented two key restrictions of AJP: first, the gelation of the deposited EC-coated graphene patterns induced by the presence of glycerol, shown in a previous work,[47] was exploited to improve resolution of high-aspect ratio features; second, the additive supported sustained atomization at relatively low voltages. This last effect has been attributed to the conformational changes of the polymer dispersants induced by the protic additive. The combination of these two effects improves resolution−deposition rate trade-offs, which is especially important during printing of high aspect ratio features. This attribute will likely be beneficial for stable deposition on nonplanar substrates, for which AJP's noncontact operation at a high standoff distance is attractive for conformal electronics and deposition on surfaces with higher roughness than those considered in this work.[56,57] Additionally, the conformational changes of the dispersing polymers might be generally exploited during formulation of other inks specifically tailored to AJP.

Finally, to demonstrate the utility of aerosol jet printed graphene, amperometric sensors were demonstrated for pesticide detection using a dipstick geometry as the device form factor. In the presence of 10 mM of acetylcholine chloride, the enzyme acetylcholinesterase on the sensor working surface became saturated and such conditions were utilized to test for parathion sensing. The printed devices are capable of sensing the pesticide, displaying a detection limit of 732 nM, thus demonstrating the viability of the current ink for application in the biotechnology industry.

## ASSOCIATED CONTENT

### Supporting Information

The Supporting Information is available free of charge at https://pubs.acs.org/doi/10.1021/acsami.2c18838.

Physicochemical properties of the chemicals used in this work together with the experimental viscosity values of the inks used in this work, additional characterization data for single-pass line profile, line resolution, and



https://doi.org/10.1021/acsami.2c18838
ACS Appl. Mater. Interfaces 2023, 15, 3325−3335

adhesion properties, as well as a representative interdigitated electrode manufactured with AJP and its characterization (PDF)

## AUTHOR INFORMATION


### Corresponding Author

**Ethan B. Secor** − *Department of Mechanical Engineering, Iowa State University, Ames, Iowa 50010, United States;* orcid.org/0000-0003-2324-1686; Email: esecor@iastate.edu

### Authors

**Livio Gamba** − *Department of Mechanical Engineering, Iowa State University, Ames, Iowa 50010, United States*

**Zachary T. Johnson** − *Department of Mechanical Engineering, Iowa State University, Ames, Iowa 50010, United States*

**Jackie Atterberg** − *Department of Mechanical Engineering, Iowa State University, Ames, Iowa 50010, United States*

**Santiago Diaz-Arauzo** − *Department of Materials Science and Engineering, Northwestern University, Evanston, Illinois 60208, United States*

**Julia R. Downing** − *Department of Materials Science and Engineering, Northwestern University, Evanston, Illinois 60208, United States*

**Jonathan C. Claussen** − *Department of Mechanical Engineering, Iowa State University, Ames, Iowa 50010, United States;* orcid.org/0000-0001-7065-1077

**Mark C. Hersam** − *Department of Materials Science and Engineering, Department of Chemistry, and Department of Electrical and Computer Engineering, Northwestern University, Evanston, Illinois 60208, United States;* orcid.org/0000-0003-4120-1426

Complete contact information is available at: https://pubs.acs.org/10.1021/acsami.2c18838


### Author Contributions

The manuscript was written through contributions of all authors. All authors have given approval to the final version of the manuscript.


### Funding

Iowa State University Department of Mechanical Engineering, Grants NSF CMMI-2037026, USDA 2021-67021-34457, USDA 2021-67011-35130, NSF ECCS-1542205, NSF DMR-1720139, State of Illinois, Bayer Crop Science.


### Notes

The authors declare no competing financial interest.

## ACKNOWLEDGMENTS


L.G. and E.B.S. acknowledge the ISU Department of Mechanical Engineering for startup funding support and access to optical profilometry equipment. The shear exfoliation of graphene with ethyl cellulose at Northwestern University was supported by the National Science Foundation Future Manufacturing Research Grant Program (Grant NSF CMMI-2037026). This work made use of the EPIC facility and Keck-II facilities of the Northwestern University NUANCE Center, which is supported by the Soft and Hybrid Nanotechnology Experimental (SHyNE) Resource (Grant NSF ECCS-1542205), the Northwestern University Materials Research Science and Engineering Center (Grant NSF DMR-1720139), and the State of Illinois. J.R.D. acknowledges financial support from the National Science Foundation (NSF) Graduate Research Fellowship Program. S.D.-A. acknowledges support from the National Consortium for Graduate Degrees for Minorities in Engineering and Science (GEM) Fellowship Program. We also acknowledge Chen Ling for data analysis support by developing an AFM analysis code available here. J.C.C. and Z.T.J. acknowledge funding support from the National Institute of Food and Agriculture, U.S. Department of Agriculture under Awards 2021-67021-34457 and 2021-67011-35130 as well as from the Grants4Ag program from Bayer Crop Science.


## ABBREVIATIONS

IBA = isobutyl acetate
Dig = diglyme
Gly = glycerol
Cyr = Cyrene
EC = ethyl cellulose
NC = nitrocellulose

## REFERENCES


(1) Hammock, M. L.; Chortos, A.; Tee, B. C. K.; Tok, J. B. H.; Bao, Z. 25th Anniversary Article: The Evolution of Electronic Skin (E-Skin): A Brief History, Design Considerations, and Recent Progress. *Adv. Mater.* **2013**, *25* (42), 5997−6038.

(2) Zymelka, D.; Yamashita, T.; Takamatsu, S.; Itoh, T.; Kobayashi, T. Thin-Film Flexible Sensor for Omnidirectional Strain Measurements. *Sens. Actuators, A* **2017**, *263*, 391.

(3) Thielen, M.; Kara, G.; Unkovic, I.; Majoe, D.; Hierold, C. Thermal Harvesting Potential of the Human Body. *J. Electron. Mater.* **2018**, *47*, 3307−3313.

(4) Braam, K.; Subramanian, V. A Stencil Printed, High Energy Density Silver Oxide Battery Using a Novel Photopolymerizable Poly(Acrylic Acid) Separator. *Adv. Mater.* **2015**, *27* (4), 689−694.

(5) Kim, J.; Imani, S.; de Araujo, W. R.; Warchall, J.; Valdés-Ramírez, G.; Paixão, T. R. L. C.; Mercier, P. P.; Wang, J. Wearable Salivary Uric Acid Mouthguard Biosensor with Integrated Wireless Electronics. *Biosens. Bioelectron.* **2015**, *74*, 1061−1068.

(6) Zhao, Y.; Gao, S.; Zhu, J.; Li, J.; Xu, H.; Xu, K.; Cheng, H.; Huang, X. Multifunctional Stretchable Sensors for Continuous Monitoring of Long-Term Leaf Physiology and Microclimate. *ACS Omega* **2019**, *4* (5), 9522−9530.

(7) Heikenfeld, J. Technological Leap for Sweat Sensing. *Nature* **2016**, *529*, 475−476.

(8) Gao, W.; Emaminejad, S.; Nyein, H. Y. Y.; Challa, S.; Chen, K.; Peck, A.; Fahad, H. M.; Ota, H.; Shiraki, H.; Kiriya, D.; Lien, D. H.; Brooks, G. A.; Davis, R.; Javey, A. Fully Integrated Wearable Sensor Arrays for Multiplexed in Situ Perspiration Analysis. *Nature* **2016**, *529*, 509−514.

(9) Craton, M. T.; Albrecht, J. T.; Chahal, P.; Papapolymerou, J. In Situ Nanocomposite Fabrication for RF Electronics Applications with Additive Manufacturing. *IEEE Trans. Microwave Theory Tech.* **2020**, *68* (5), 1646−1659.

(10) Kamyshny, A.; Magdassi, S. Conductive Nanomaterials for Printed Electronics. *Small* **2014**, *10* (17), 3515−3535.

(11) Grau, G.; Cen, J.; Kang, H.; Kitsomboonloha, R.; Scheideler, R.; Subramanian, V. Gravure-Printed Electronics: Recent Progress in Tooling Development, Understanding of Printing Physics, and Realization of Printed Devices. *Flexible Printed Electron.* **2016**, *1*, 023002.

(12) Secor, E. B.; Lim, S.; Zhang, H.; Frisbie, C. D.; Francis, L. F.; Hersam, M. C. Gravure Printing of Graphene for Large-Area Flexible Electronics. *Adv. Mater.* **2014**, *26* (26), 4533−4538.

(13) Khan, Y.; Thielens, A.; Muin, S.; Ting, J.; Baumbauer, C.; Arias, A. C. A New Frontier of Printed Electronics: Flexible Hybrid Electronics. *Adv. Mater.* **2020**, *32*, 1905279.

(14) Feng, J. Q.; Renn, M. J. Aerosol Jet Direct-Write for Microscale Additive Manufacturing. *Journal of Micro- and Nano-Manufacturing* **2019**, *7*, 011004.
(15) Secor, E. B. Principles of Aerosol Jet Printing. *Flexible Printed Electron.* **2018**, *3*, 035002.
(16) Xie, W.; Zhang, X.; Leighton, C.; Frisbie, C. D. 2D Insulator−Metal Transition in Aerosol-Jet-Printed Electrolyte-Gated Indium Oxide Thin Film Transistors. *Adv. Electron. Mater.* **2017**, *3* (3), 1600369.
(17) Reitberger, T.; Hoffmann, G. A.; Wolfer, T.; Overmeyer, L.; Franke, J. Printing Polymer Optical Waveguides on Conditioned Transparent Flexible Foils by Using the Aerosol Jet Technology. *Proc. SPIE* **2016**, *9945*, 99450G.
(18) You, R.; Liu, Y.-Q.; Hao, Y.-L.; Han, D.-D.; Zhang, Y.-L.; You, Z. Laser Fabrication of Graphene-Based Flexible Electronics. *Adv. Mater.* **2020**, *32* (15), 1901981.
(19) Kim, S. J.; Choi, K.; Lee, B.; Kim, Y.; Hong, B. H. Materials for Flexible, Stretchable Electronics: Graphene and 2D Materials. *Annu. Rev. Mater. Res.* **2015**, *45*, 63−84.
(20) Pola, C. C; Rangnekar, S. V; Sheets, R.; Szydłowska, B. M; Downing, J. R; Parate, K. W; Wallace, S. G; Tsai, D.; Hersam, M. C; Gomes, C. L; Claussen, J. C Aerosol-Jet-Printed Graphene Electrochemical Immunosensors for Rapid and Label-Free Detection of SARS-CoV-2 in Saliva. *2D Mater.* **2022**, *9* (3), 035016.
(21) Parate, K.; Pola, C. C.; Rangnekar, S. V.; Mendivelso-Perez, D. L.; Smith, E. A.; Hersam, M. C.; Gomes, C. L.; Claussen, J. C. Aerosol-Jet-Printed Graphene Electrochemical Histamine Sensors for Food Safety Monitoring. *2D Mater.* **2020**, *7* (3), 034002.
(22) Parate, K.; Rangnekar, S. V.; Jing, D.; Mendivelso-Perez, D. L.; Ding, S.; Secor, E. B.; Smith, E. A.; Hostetter, J. M.; Hersam, M. C.; Claussen, J. C. Aerosol-Jet-Printed Graphene Immunosensor for Label-Free Cytokine Monitoring in Serum. *Appl. Mater. Interfaces* **2020**, *12*, 8592−8603.
(23) Donnelly, T. D.; Hogan, J.; Mugler, A.; Schubmehl, M.; Schommer, N.; Bernoff, A. J.; Dasnurkar, S.; Ditmire, T. Using Ultrasonic Atomization to Produce an Aerosol of Micro-Scale Particles. *Rev. Sci. Instrum.* **2005**, *76*, 113301.
(24) Lozano, A.; Garcia, J. A.; Navarro, J. L.; Calvo, E.; Barreras, F. Influence of Viscosity on Droplet Size Distrubution and Generation Rate in Ultrasonic Atomization. *Atomization Sprays* **2010**, *20* (11), 923−934.
(25) Feng, J. Q. Vapor Transport of a Volatile Solvent for a Multicomponent Aerosol Droplet. *Aerosol Sci. Technol.* **2015**, *49* (9), 757−766.
(26) Neagu, R.; Perednis, D.; Princivalle, A.; Djurado, E. Zirconia Coatings Deposited by Electrostatic Spray Deposition A Chemical Approach. *Solid State Ionics* **2006**, *177*, 1451−1460.
(27) Eyer, F.; Meischner, V.; Kiderlen, D.; Thiermann, H.; Worek, F.; Haberkorn, M.; Felgenhauer, N.; Zilker, T.; Eyer, P. Human Parathion Poisoning. *Toxicol. Rev.* **2003**, *22* (3), 143−163.
(28) Garcia, S.; Abu-Qare, A.; Meeker-O'Connell, W.; Borton, A.; Abou-Donia, M. Methyl Parathion: A Review of Health Effects. *J. Toxicol. Environ. Health, Part B* **2003**, *6*, 185−210.
(29) Secor, E. B.; Hersam, M. C. Emerging Carbon and Post-Carbon Nanomaterial Inks for Printed Electronics. *J. Phys. Chem. Lett.* **2015**, *6*, 620.
(30) Sui, X.; Downing, J. R.; Hersam, M. C.; Chen, J. Additive Manufacturing and Applications of Nanomaterial-Based Sensors. *Mater. Today* **2021**, *48*, 135−154.
(31) Secor, E. B.; Prabhumirashi, P. L.; Puntambekar, K.; Geier, M. L.; Hersam, M. C. Inkjet Printing of High Conductivity, Flexible Graphene Patterns. *J. Phys. Chem. Lett.* **2013**, *4*, 1347−1351.
(32) Tafoya, R. R.; Gallegos, M. A.; Downing, J. R.; Gamba, L.; Kaehr, B.; Coker, E. N.; Hersam, M. C.; Secor, E. B. Morphology and Electrical Properties of High-Speed Flexography-Printed Graphene. *Microchim. Acta* **2022**, *189*, 123.
(33) Subramanian, V.; Cen, J.; de la Fuente Vornbrock, A.; Grau, G.; Kang, H.; Kitsomboonloha, R.; Soltman, D.; Tseng, H. Y. High-Speed Printing of Transistors: From Inks to Devices. *Proc. IEEE* **2015**, *103* (4), 567−682.
(34) Secor, E. B.; Gao, T. Z.; Islam, A. E.; Rao, R.; Wallace, S. G.; Zhu, J.; Putz, K. W.; Maruyama, B.; Hersam, M. C. Enhanced Conductivity, Adhesion, and Environmental Stability of Printed Graphene Inks with Nitrocellulose. *Chem. Mater.* **2017**, *29* (5), 2332−2340.
(35) Ferrari, A. C.; Basko, D. M. Raman Spectroscopy as a Versatile Tool for Studying the Properties of Graphene. *Nat. Nanotechnol.* **2013**, *8*, 235−346.
(36) Green, A. A.; Hersam, M. C. Solution Phase Production of Graphene with Controlled Thickness via Density Differentiation. *Nano Lett.* **2009**, *9* (12), 4031−4036.
(37) Gao, W.; Alemany, L. B.; Ci, L.; Ajayan, P. M. New Insights into the Structure and Reduction of Graphite Oxide. *Nat. Chem.* **2009**, *1*, 403−408.
(38) Ferrari, A. C. Raman Spectroscopy of Graphene and Graphite: Disorder, Electron−Phonon Coupling, Doping and Nonadiabatic Effects. *Solid State Commun.* **2007**, *143*, 47−57.
(39) Das, S. R.; Nian, Q.; Cargill, A. A.; Hondred, J. A.; Ding, S.; Saei, M.; Cheng, G. J.; Claussen, J. C. 3D Nanostructured Inkjet Printed Graphene via UV-Pulsed Laser Irradiation Enables Paper-Based Electronics and Electrochemical Devices. *Nanoscale* **2016**, *8*, 15870−15879.
(40) de Moraes, A. C. M.; Obrzut, J.; Sangwan, V. K.; Downing, J. R.; Chaney, L. E.; Patel, D. K.; Elmquist, R. E.; Hersam, M. C. Elucidating Charge Transport Mechanisms in Cellulose-Stabilized Graphene Inks. *J. Mater. Chem. C* **2020**, *8*, 15086−15091.
(41) Paton, K. R.; et al. Scalable Production of Large Quantities of Defect-Free Few-Layer Graphene by Shear Exfoliation in Liquids. *Nat. Mater.* **2014**, *13*, 624−360.
(42) Reichardt, C. Properties of Solvents Used in Organic Chemistry, 2020. http://murov.info/orgsolvents.htm.
(43) Wang, Z.; Orejon, D.; Takata, Y.; Sefiane, K. Wetting and Evaporation of Multicomponent Droplets. *Phys. Rep.* **2022**, *960*, 1−37.
(44) Surface Tension Values of Some Common Test Liquids for Surface Energy Analysis, 2017. http://www.surface-tension.de/.
(45) Sherwood, J.; De Bruyn, M.; Constantinou, A.; Moity, L.; McElroy, C. R.; Farmer, T. J.; Duncan, T.; Raverty, W.; Hunt, A. J.; Clark, J. H. Dihydrolevoglucosenone (Cyrene) as a Bio-Based Alternative for Dipolar Aprotic Solvents. *Chem. Commun.* **2014**, *50*, 9650−9652.
(46) Salavagione, H. J.; Sherwood, J.; De Bruyn, M.; Budarin, V. L.; Ellis, G. J.; Clark, J. H.; Shuttleworth, P. S. Identification of High Performance Solvents for the Sustainable Processing of Graphene. *Green Chem.* **2017**, *19*, 2550.
(47) Secor, E. B.; Dos Santos, M. H.; Wallace, S. G.; Bradshaw, N. P.; Hersam, M. C. Tailoring the Porosity and Microstructure of Printed Graphene Electrodes via Polymer Phase Inversion. *J. Phys. Chem. C* **2018**, *122* (25), 13745−13750.
(48) Secor, E. B. Guided Ink and Process Design for Aerosol Jet Printing Based on Annular Drying Effects. *Flex. Print. Electron.* **2018**, *3* (3), 035007.
(49) Papaioannou, D.; Evangelou, T.; Panayiotou, C. Dynamic Viscosity of Multicomponent Liquid Mixtures. *J. Chem. Eng. Data* **1991**, *36*, 43−46.
(50) Ratcliff, G. A.; Khan, M. A. Prediction of the Viscosities of Liquid Mixtures by a Group Solution Model. *Can. J. Chem. Eng.* **1971**, *49*, 125−129.
(51) Tafoya, R. R.; Secor, E. B. Understanding Effects of Printhead Geometry in Aerosol Jet Printing. *Flexible Printed Electron.* **2020**, *5*, 035004.
(52) Arapov, K.; Bex, G.; Hendriks, R.; Rubingh, E.; Abbel, R.; de With, G.; Friedrich, H. Conductivity Enhancement of Binder-Based Graphene Inksby Photonic Annealing and Subsequent Compression Rolling. *Adv. Eng. Mater.* **2016**, *18* (7), 1234−1239.
(53) Hondred, J. A.; Medintz, I. L.; Claussen, J. C. Enhanced Electrochemical Biosensor and Supercapacitor with 3D Porous

Architectured Graphene via Salt Impregnated Inkjet Maskless Lithography. *Nanoscale Horiz.* **2019**, *4*, 735−746.
(54) Mehta, J.; Vinayak, P.; Tuteja, S. K.; Chhabra, V. A.; Bhardwaj, N.; Paul, A. K.; Kim, K.-H.; Deep, A. Graphene Modified Screen Printed Immunosensor for Highly Sensitive Detection of Parathion. *Biosens. Bioelectron.* **2016**, *83*, 339−346.
(55) Huang, X.-J.; O'Mahony, A. M.; Compton, R. G. Microelectrode Arrays for Electrochemistry: Approaches to Fabrication. *Small* **2009**, *5* (7), 776−788.
(56) Paulsen, J. A.; Renn, M.; Christenson, K.; Plourde, R. Printing Conformal Electronics on 3D Structures with Aerosol Jet Technology. *2012 Future of Instrumentation International Workshop (FIIW) Proceedings*; IEEE, 2012; pp 1−4, DOI: 10.1109/FIIW.2012.6378343.
(57) Kaindl, R.; Gupta, T.; Blümel, A.; Pei, S.; Hou, P.-X.; Du, J.; Liu, C.; Patter, P.; Popovic, K.; Dergez, D.; Elibol, K.; Schafler, E.; Liu, J.; Eder, D.; Kieslinger, D.; Ren, W.; Hartmann, P.; Waldhauser, W.; Bayer, B. C. Aerosol Jet Printing of Graphene and Carbon Nanotube Patterns on Realistically Rugged Substrates. *ACS Omega* **2021**, *6* (50), 34301−34313.





https://doi.org/10.1021/acsami.2c18838
*ACS Appl. Mater. Interfaces* 2023, 15, 3325−3335